How to cite: *Angew. Chem. Int. Ed.* **2023,** *62,* e202218717
International Edition: doi.org/10.1002/anie.202218717
German Edition: doi.org/10.1002/ange.202218717

Electrocatalysis

Enabled Efficient Ammonia Synthesis and Energy Supply in a Zinc–Nitrate Battery System by Separating Nitrate Reduction Process into Two Stages

Haifeng Jiang, Gao-Feng Chen, Oleksandr Savateev, Jian Xue, Liang-Xin Ding, Zhenxing Liang, Markus Antonietti, and Haihui Wang**

Abstract: The aqueous electrocatalytic reduction of NO_3^- into NH_3 (NitrRR) presents a sustainable route applicable to NH_3 production and potentially energy storage. However, the NitrRR involves a directly eight-electron transfer process generally required a large overpotential (<-0.2 V versus reversible hydrogen electrode (*vs.* RHE)) to reach optimal efficiency. Here, inspired by biological nitrate respiration, the NitrRR was separated into two stages along a [2+6]-electron pathway to alleviate the kinetic barrier. The system employed a Cu nanowire catalyst produces NO_2^- and NH_3 with current efficiencies of 91.5 % and 100 %, respectively at lower overpotentials ($>+0.1$ *vs.* RHE). The high efficiency for such a reduction process was further explored in a zinc-nitrate battery. This battery could be specified by a high output voltage of 0.70 V, an average energy density of 566.7 Wh L^{-1} at 10 mA cm^{-2} and a power density of 14.1 mW cm^{-2}, which is well beyond all previously reported similar concepts.

Ammonia (NH_3), has been technically synthesized by the traditional Haber-Bosch process over the past century and is extensively used in fertilizers production; ammonia is also regarded as an emerging carbon-free liquid fuel.[1] Currently, the growing applications have accumulated to a global demand for ammonia over 170 million tons per year, which is predicted to increase annually by 2.3 % in the future.[1d,2] However, the Haber-Bosch process with operating at high temperature and pressure accounts for 1–2 % of the global energy consumption, while being associated with 1.5 % of the global CO_2 emission due to the use of methane as a hydrogen source.[3] To make the process of nitrogen fixation more energy-efficient and environmentally friendly, an electro-assisted route for nitrogen reduction reaction (NRR) using water as a hydrogen source has been actively explored over the past few years.[4] Unfortunately, there are still some rather fundamental scientific challenges, such as the minor solubility of N_2 in aqueous electrolytes (6.8×10^{-4} M in water) and the demanding activation of the N≡N triple bond (914 kJ mol^{-1}) for NRR at ambient conditions, reflected in dissatisfactory production rates and selectivity (Table S1).[4b,5] From this perspective, it is vital to find an appealing and sustainable N-containing alternative for ammonia production.

Recently, various nitrogen sources, such as nitric oxide (NO), nitrite (NO_2^-), nitrate (NO_3^-), and mixtures of nitrogen oxide (NO_x) generation via non-thermal plasma were considered promising (local recycling) alternatives due to the low binding energy of N=O (204 kJ mol^{-1}).[6] Especially, NO_3^-, showing absolute solubility in water and as one of the most widespread groundwater pollutants in the world, is more highly attractive to be utilized to produce the value-added NH_3 from the environmental perspective.[7] The theoretical energy consumption of ammonia electrosynthesis from NO_3^- (NitrRR) is calculated to be 6.5 kWh kg^{-1} (pH = 14), which is lower than that of the Haber-Bosch method (10–13 kWh kg^{-1}) from N_2.[8] Therefore, extensive experimental endeavors, including optimizing catalysts and electrolytes, have recently been pursued to achieve a high yield rate and current efficiency. However, to complete an $8H^+/8e^-$-transfer process, almost all systems were inevitably bound to a significant negative potential of <-0.2 V versus reversible hydrogen electrode (*vs.* RHE), which translates into a high energy consumption of 21–38 kWh kg^{-1} to obtain optimal efficiency due to the slow kinetics inherent of NitrRR (Table S2).[6f,9]

Fortunately, biological denitrification in Nature provides a more efficient solution to accelerating kinetics of the NitrRR. The nitrate respiration for energy release in bacteria is separated into two stages, consisting first of the

[*] H. Jiang, Dr. G.-F. Chen, Dr. J. Xue, Prof. L.-X. Ding, Prof. Z. Liang
School of Chemistry and Chemical Engineering, South China University of Technology
Guangzhou 510640 (China)
H. Jiang, Prof. H. Wang
Beijing Key Laboratory for Membrane Materials and Engineering, Department of Chemical Engineering, Tsinghua University
Beijing 100084 (China)
E-mail: cehhwang@tsinghua.edu.cn
Dr. G.-F. Chen, Dr. O. Savateev, Prof. M. Antonietti
Department of Colloid Chemistry, Max-Planck Institute of Colloids and Interfaces, Research Campus Golm
Am Mühlenberg 1, 14476 Potsdam (Germany)
E-mail: gaofeng.chen@mpikg.mpg.de

conversion of nitrate to nitrite (NO_2^-) by a nitrate reductase, then promoting the reduction of nitrite to NO or ammonium with nitrite reductases (Figure 1a).[10] This naturally occurring pathway, has been utilized in biological processes for several hundred million years and points to our opinion to an evolutionary optimized reaction path, i.e. it can be considered a viable method for customizing artificial nitrate respiration in an energy-efficient way.

In this work, by mimicking the two-stage process of nitrate respiration in bacteria, an indirect electrocatalytic NitrRR with a [2+6]-electron pathway was proposed and realized using a Cu-nanowire-arrays catalyst. The system enables low overpotentials for both nitrite synthesis (+0.2 V *vs.* RHE) and for ammonia synthesis (+0.1 V *vs.* RHE) with Faradaic efficiencies (FE) of 91.5 % and 100 %, respectively. Accordingly, an integrated energy consumption of 17.7 kWh kg^{-1} was calculated, which is comparable with the traditional Haber–Bosch process. In addition, considering the final practical application of nitrate reduction to produce ammonia requires operation in a two-electrode system and several research works recently demonstrated a highly attractive application of combining the NitrRR-based cath-

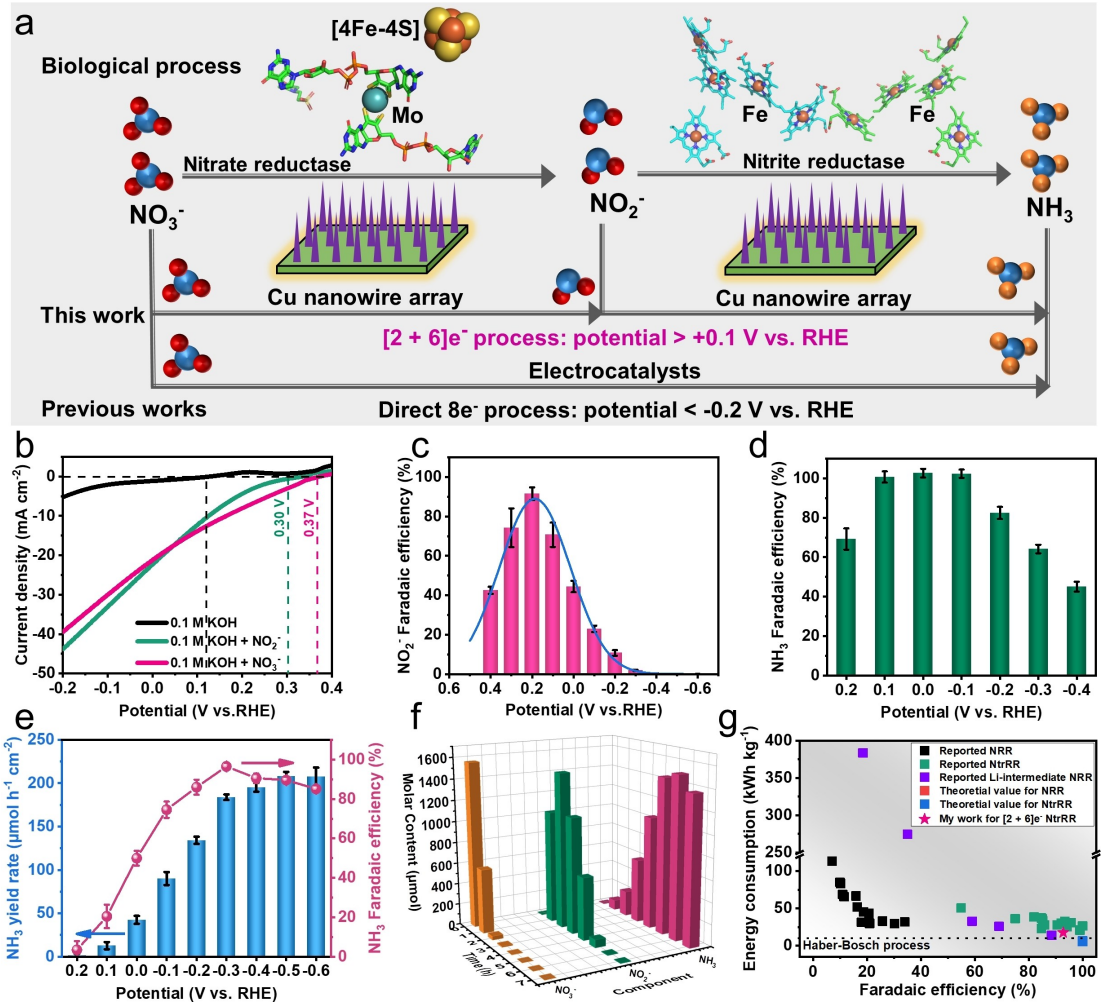

Figure 1. Achieving efficient ammonia production at lower overpotential by mimicking the two-stage reduction process of biological nitrate respiration to accomplish the [2+6]-electron pathway. a) Schematic illustration of nitrate reduction in the biological process, the mimicked [2+6]-electron pathway in this work and the reported direct eight-electron route. In nitrate reductase, the molybdenum site conjugated to two molybdopterin guanosine dinucleotide (MGD) and formed $(MGD)_2Mo$ cofactors. (Carbon atom, green; hydrogen atom, gray; nitrogen atom, blue; oxygen atom, red; sulfur atom, orange; molybdenum, dark green sphere). For the [4Fe-4S] cluster of nitrate reductase, yellow and orange spheres represent the S and Fe atoms, respectively.[10a] In cytochrome c nitrite reductase (haem arrangement), orange spheres represent active-site Fe atoms.[10b] b) Magnifying linear sweep voltammetry curves of Cu-RD-KOH electrocatalysts for NO_3^--to-NH_3 and NO_2^--to-NH_3 conversions recorded in various electrolytes (0.1 M KOH solution, 0.1 M KOH solution contained 4000 ppm nitrite and 0.1 M KOH solution contained 4000 ppm nitrate). c) Faradaic efficiency for reduction of NO_3^- to NO_2^- by employing Cu-RD-KOH electrode in 500 ppm NO_3^-/0.1 M KOH electrolyte after 2-hour electrolysis. d) Faradaic efficiency for the reduction of NO_2^- to NH_3 at different potentials in 371 ppm NO_2^-/0.1 M KOH electrolyte. e) Yield rate and Faradaic efficiency of the reduction of NO_3^- to NH_3 at different potentials applied potentials in 500 ppm NO_3^-/0.1 M KOH electrolyte. f) The time-dependent concentration profile of the original NO_3^- and produced NO_2^- and NH_3 using 2000 ppm NO_3^-/0.1 M KOH solution as electrolyte and applying a potential of −0.3 V vs. RHE. g) Comparison of energy consumption and Faradaic efficiency among our system, the Haber-Bosch process, NRR and NitrRR process.

ode with metal anode as a galvanic cell for simultaneous energy supply and ammonia production.[9c,11] Therefore, this work also assembled an aqueous battery by combining a nitrate cathode with a zinc anode (Zn–NO_3^- battery). Benefitting from the staged [2+6]-electron pathway, the Zn–NO_3^- battery enabled efficient energy supply with the highest output voltage of 0.70 V, an energy density of 566.7 Wh L^{-1} at 10 mA cm^{-2} and a power density of 14.1 mW cm^{-2}, which are far higher than recently reported state-of-the-art results using a direct eight-electron transfer process.

Various metal-based catalysts (including Ru, Pd, Cu, Co, Ni and Fe) and their composites have been developed over the years to selectively convert NO_3^- to NH_3.[9a,d,12] Among them, the NO_2^- intermediate was usually detected when employing Cu-based catalysts. Therefore, to mimic the staged [2+6]-electron pathway of biological nitrate respiration, here a Cu nanowire array catalyst was synthesized, in which several prerequisites were satisfied to achieve either fast reaction kinetics or high efficiency: i) Cu nanowire arrays are self-grown from the surface of Cu foam, which guarantees the strong integration of current collector and catalyst, and then ensures high conductivity and structural stability of the electrode. ii) A nanowire array structure facilitates the rapid transport and diffusion of reactants, intermediates and products across the electrode surface. iii) The Cu nanowire array being composed of pure Cu^0 was synthesized through an electrochemical pre-reduction process at −0.4 V *vs.* RHE in 0.1 M KOH solution (defined as Cu-RD-KOH), which separates a potential reduction of the electrode itself to guarantee 100 % of the applied current for the NitrRR.

The feasibility of this electrode and the staged [2+6]-electron pathway to accelerate the reaction kinetics was first evaluated roughly through linear sweep voltammetry (LSV) tests. The LSV curves of Cu-RD-KOH exhibit an onset potential (the cathodic potential at −0.1 mA cm^{-2}) of ≈ +0.4 V *vs.* RHE in NO_3^--containing electrolyte and an onset potential ≈ +0.3 V *vs.* RHE in a NO_2^--containing electrolyte (Figures 1b and S1, S2), which represent the initial reduction of NO_3^- and NO_2^-, respectively and indicate the potentials separately used for the conversion of NO_3^- to NO_2^- and NO_2^- to NH_3. It is more positive than that reported for the direct conversion of NO_3^- to NH_3 by the eight-electron transfer process (Table S3). This conjecture was confirmed when we sought to quantitatively evaluate the synthesis of NO_2^- and NH_3 operating in a 0.1 M KOH solution containing 500 ppm NO_3^- at a series of potentials with a reaction time of two hours. The detail descriptions for quantitative detection of NO_2^- and NH_3 can be seen in the experimental procedures of Supporting Information. The two-electron transfer step for the conversion of NO_3^- to NO_2^- is prevailing as potentials ranging from +0.4 to +0.1 V *vs.* RHE and obtains a maximum FE of 91.5 ± 3.2 % at a potential of +0.2 V *vs.* RHE (Figures 1c and S6, S7). After all of NO_3^- is converted to NO_2^-, the further production of NH_3 only requires a potential of +0.1 V *vs.* RHE to achieve a FE of 100.7 ± 2.8 % (Figures 1d and S8). Therefore, from the point of view of energy use, the two-stage reduction process by the [2+6]-electron pathway is more favorable compared to the direct NH_3 synthesis by the eight-electron transfer process (< −0.2 V *vs.* RHE, Table S4).

The NitrRR catalyzed by the Cu-RD-KOH electrode at a more reductive potential of −0.3 V *vs.* RHE seems to follow a straightforward eight-electron process, and very high FE (96.5 ± 1.9 %) for NH_3 production was found (Figures 1e and S9, S10). The optimal potential also agrees well with the typical potential used to achieve the highest efficiency for direct NH_3 synthesis in previously reported systems (Table S4). We assume that the mechanism also follows the staged [2+6]-electron pathway, it is just that the higher overpotential is not absolutely needed for the NO_2^--to-NH_3 reaction, but the current is consumed, nevertheless. As that, the 500 ppm NO_3^- in electrolyte is converted mostly to NH_3 after two hours of reaction time. Two facts support this conclusion: i) More than 90 % conversion after a two-hour NitrRR process at potentials below +0.1 V *vs.* RHE can be reported (Figure S11c). However, NO_2^- can always be detected at more positive potentials higher than −0.3 V *vs.* RHE (Figures S6 and S7). Finally, for potentials more negative than −0.3 V *vs.* RHE, both NO_3^- and NO_2^- intermediates are converted to NH_3, and H_2 evolution reaction begins to prevail (Figures S12–14). ii) A series of NO_3^- concentrations from 20 to 2000 ppm were also studied at −0.3 V *vs.* RHE under otherwise unchanged conditions (Figure S15). At a NO_3^- concentration of 500 ppm or below, no NO_2^- could be detected. When the concentration of NO_3^- exceeds 500 ppm, a larger amount of NO_2^- intermediate was observed. For example, at 2000 ppm NO_3^-, NO_2^- intermediate in electrolyte reached a maximum concentration (90.8 % of NO_3^- turned to NO_2^-) after two-hour electrolysis, simply underlining that NO_3^- binds stronger to the active sites, in spite of a lower overpotential needed for NO_2^- reduction. This phase is followed by the almost complete conversion of NO_2^- to NH_3 after six-hour electrolysis (Figures 1f and S16). The higher substrate binding also reflects in the rate constants. The two-electron pathway delivers a rate constant of ≈1.19 h^{-1} during the initially two-hour electrolysis, while the apparent rate constant for the one-step conversion of NO_3^- to NH_3 is 0.08 h^{-1}. Using the second phase of reaction, the dominating six-electron pathway can be described by a rate constant of ≈1.34 h^{-1} (Figure S17). Therefore, nitrate reduction to nitrite via a 2-electron transfer process preferentially occurs in the presence of nitrate in electrolyte, most of which desorb from the surface of catalyst. And the increasing production of NH_3 from the reduction of re-absorbed nitrite on the catalyst surface is visible only after most of nitrate is converted to nitrite, which indicates nitrate acts as an inhibitor for nitrite-reduction.

As also Nature uses a two-enzyme, staged [2+6]-electron pathway to convert all the NO_3^- to NO_2^- and then to convert the NO_2^- to NH_3. We assume that similar overpotential and inhibition considerations also hold true for the biological system.[13] As a consequence, we can visualize the advantage of staged [2+6]-electron pathway of the technical mimic in terms of energy consumption. A low integrated

energy consumption of 17.7 kWh kg^{-1} can be calculated for the staged [2+6]-electron pathway, being far lower than that in this work (23.5 kWh kg^{-1}) by a complete one-step conversion of NO_3^- to NH_3 and in previously reported system (21–38 kWh kg^{-1}) (Figure 1g and Table S2).

The active components of Cu-RD-KOH catalyst play an important role to control the process of NH_3 synthesis. The primary Cu nanowire array was self-grown from copper foam by successive electropolishing and thermal annealing of copper foam (defined as CF-A, Figures S18–22),[14] and contains mixed components of Cu^0, Cu_2O and CuO (Figures 2m, S23 and Note S4). The Cu-RD-KOH electrode was then prepared by electrochemical pre-reduction of the primary Cu nanowire electrode at −0.4 V *vs.* RHE in a 0.1 M KOH solution. As shown in transmission electron microscopy (TEM) images, selected-area electron diffraction patterns (SAED), elemental mapping images, X-ray diffraction (XRD) patterns, and X-ray photoelectron spectroscopy (XPS) (Figures 2e–h and 2l–n, see detailed discussion in Note S1), the catalyst then only contain pure Cu^0 components, which avoids the consumption of electrons by self-reduction of catalyst and promote a high FE even at more positive potentials.

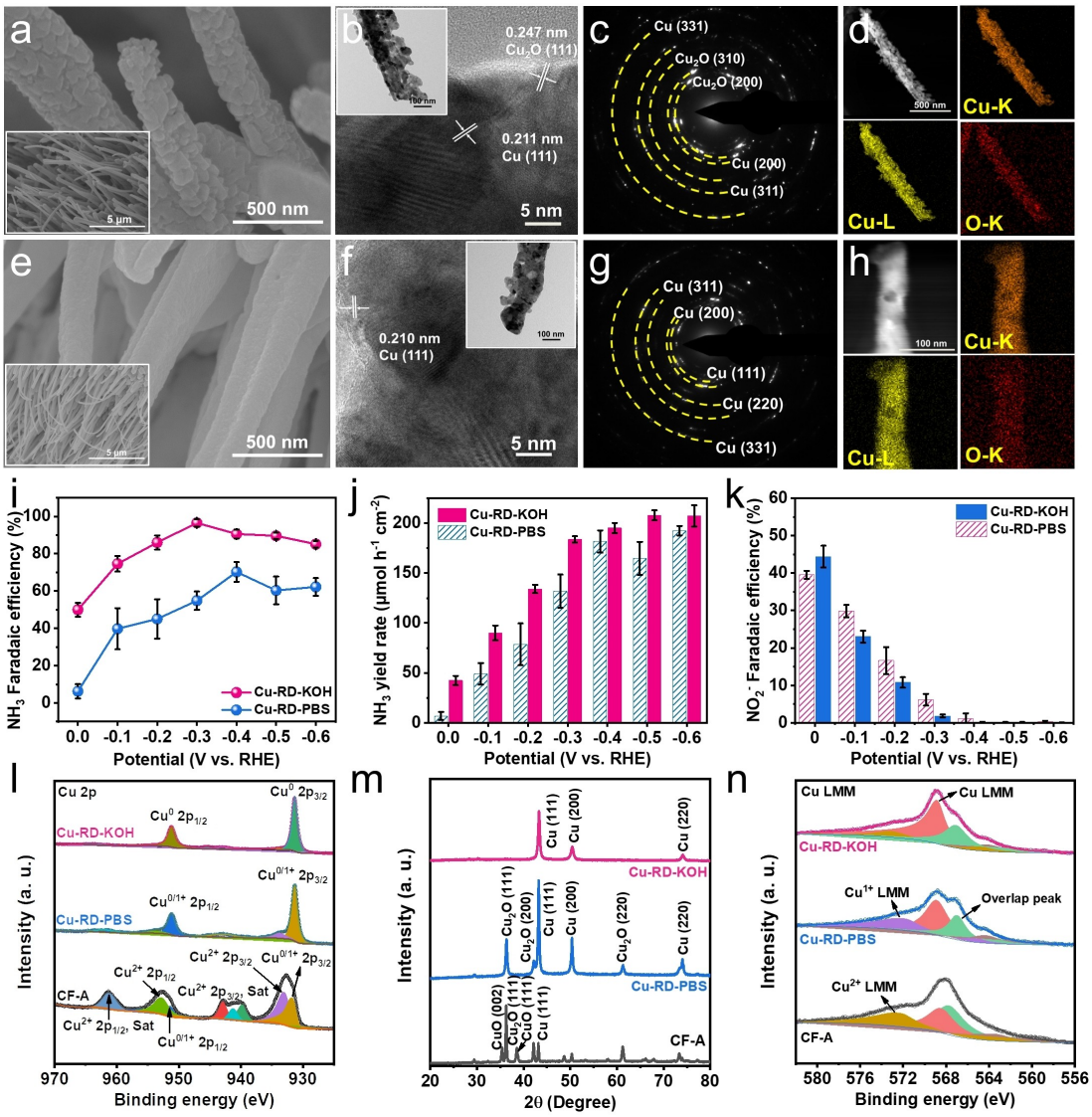

Figure 2. Structural characterizations and identification of active sites for the NitrRR. a)–d) Morphology characterizations of Cu-RD-PBS. a) SEM images at a different scale bar. b) TEM and HRTEM images. c) The corresponding SAED. d) The corresponding elemental mapping images. Morphology characterization of Cu-RD-KOH electrode from e) to h). e) SEM images at two scale bars. f) The corresponding HRTEM image. The inset of f) is the corresponding TEM image. g) SAED pattern. h) STEM and elemental mapping images. i)–k) Comparison of the NitrRR performance when using the Cu-RD-PBS and Cu-RD-KOH electrodes. i) NH_3 Faradaic efficiency. j) NH_3 yield rate. k) NO_2^- Faradaic efficiency after two-hour reaction with original NO_3^- concentration of 500 ppm at different potentials. l)–n) Further structural and composition characterization of Cu-based catalysts. l) Deconvoluted Cu 2p region of XPS spectra. m) XRD patterns. n) Cu LMM auger XPS spectra of samples under different pretreated conditions.

For comparison, the CF-A was also pre-reduced at −0.4 V *vs.* RHE in a 0.1 M PBS solution (defined as Cu-RD-PBS), which retained a considerable amount of Cu_2O (Figures 2a–d). Obviously, a relatively poor performance of Cu-RD-PBS with its mixed components of Cu^0 and Cu_2O was observed (Figures 2i–k), which suggests that i) a pure Cu^0 component is responsible for the enhanced NitrRR performance (Figures S24–28) and ii) the contained Cu_2O acts as a heterojunction to reduce the electron activity in the mixture.

To further clarify the reduction behavior of Cu_2O in the NitrRR process, ex situ XRD and infrared spectroscopy of the Cu-RD-PBS electrode after testing the NitrRR at certain time intervals were applied. Both the ex situ XRD and infrared absorption spectroscopy show the slow vanishing of Cu_2O with the increase of reaction time, and after 100 min, the Cu_2O peak completely disappears (Figures 3a and 3b). Only nanowire arrays built from pure Cu^0 components showed the preferable efficiency to complete the staged [2+6]-electron process for NH_3 synthesis (Figure 3c).[6f]

Density functional theory (DFT) calculations were carried out to gain an in-depth understanding of the [2+6]-electron pathway in Cu-RD-KOH electrode (Figures 3d–f). According to the results of TEM and XRD, the Cu (111) facets, representing Cu-RD-KOH, were chosen as reaction interfaces. Referring to the NitrRR, there are three possible NO_3^- reduction pathways including NO_2^-, NH_3 and N_2 products. The free energy of the NO_3^- activation and subsequent hydrogenation steps on Cu (111) facet are mostly exothermic except for the NO_2^- and NH_3 desorption (Figures 3d and S29, S30). The NH_3 desorption (0.6 eV) is more thermodynamically hindered compared with the desorption of $*NO_2$ intermediate to form NO_2^- (0.4 eV), explaining the competing function of NO_3^- reduction to NO_2^- on NO_2^- reduction to NH_3 and the possible realization

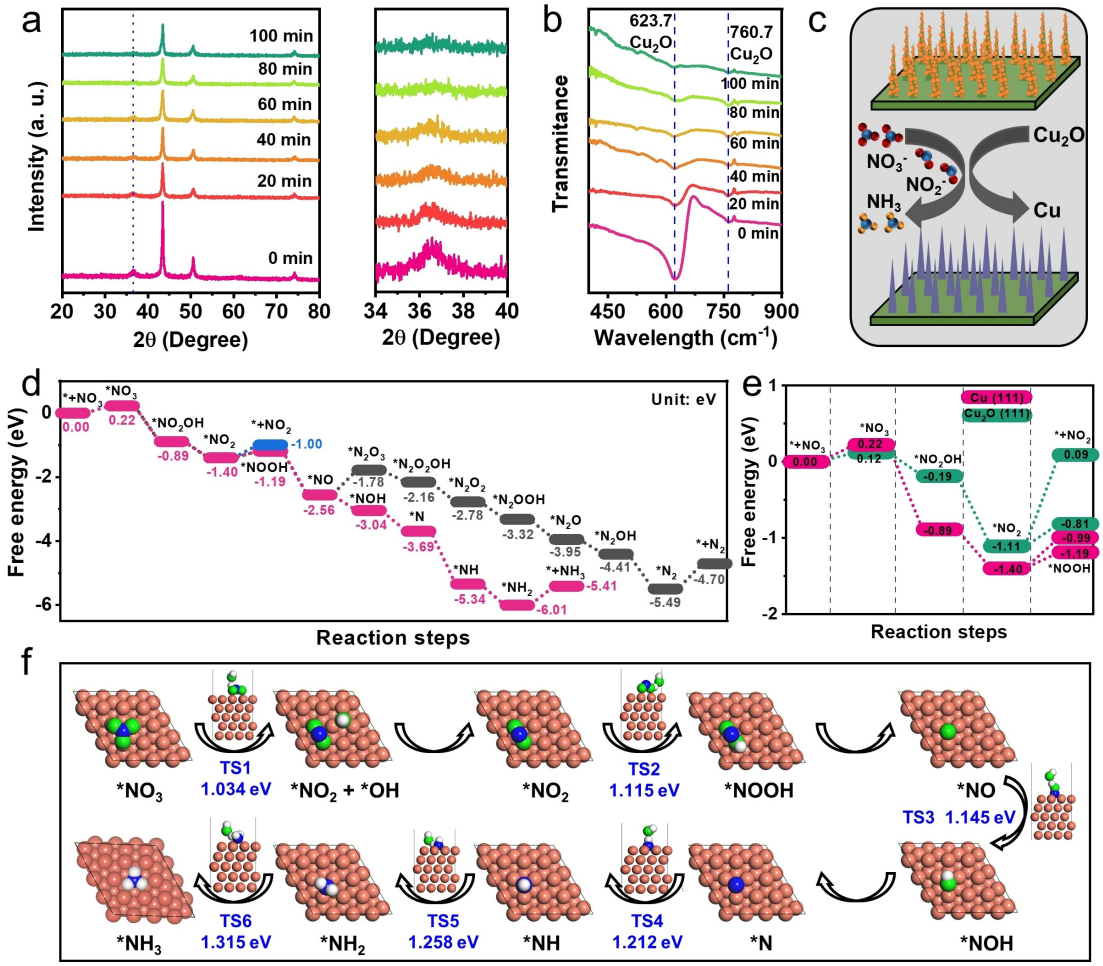

Figure 3. Verifying Cu active sites for NitrRR and understanding [2+6]-electron pathway of NitrRR process by density functional theory calculations. a)–c) Further identifying active catalytic sites for the NitrRR. a) ex situ XRD pattern and b) The collected infrared absorption spectrum of the Cu-RD-PBS with the increasing reduction time at −0.3 V vs. RHE. c) Schematic representation for the transformation of Cu active sites. d) Reaction free energy of different intermediates for NO_3^- reduction reaction on Cu (111) surface of Cu-RD-KOH with an applied potential of U = 0 V. The red represents the [2+6]-electron transfer form NO_3^- to NH_3. The blue line represents the possible reaction pathway for NO_2^- formation by two-electron transfer. The brown line is the pathway for reducing of NO_3^- to 1/2 N_2 via a five-electron transfer. e) The comparison of the free energy diagram for the reduction of NO_3^- into NO_2^- and *NOOH over Cu (111) and Cu_2O (111) at an applied potential of U = 0 V. f) Simulated atomistic structure scheme shows a reaction pathway for the reduction of NO_3^- to NH_3 and the corresponding transition state (TS) energy barriers.

of the staged [2+6]-electron pathway in the presence of nitrates inhibitor. The results are consistent with that of many previously reported systems using Cu-based catalysts.[12e,15] Namely, NH_3 desorption is the rate-determination step, resulting in the formation of nitrite intermediates often found when Cu-based catalysts were used. In contrast, some systems used Ni- and Co-based catalyst were found that NH_3 desorption is an exothermic process.[9d,16] Thereby NO_2^- intermediates were rarely detected and NO_3^- reduction to NH_3 via direct eight-electron transfer process was dominant in these systems, which explained why these systems required a high overpotential to drive the NH_3 synthesis process.

In addition, we can see that the dimerization of intermediates for $*N_2O_3$ formation is clearly uphill where incorporation of the solvated NO_2^- is necessary, so the path towards N_2 generation is blocked. This, combined with the lower Gibbs energy barrier (ΔG) for water surface homolysis into *H and *OH (Figure S31) to facilitate the hydrogenation steps, which explains the obtained experimental results why NO_3^- reduction into NH_3 is more favorable than the N_2 generation: it is with two exceptions a simple downhill cascade. In addition, higher transition state energy barriers to form the possible intermediates ($*N_2O_3$, N_2O_2, N_2, and N_2H_4) in the pathway of N_2 formation are required (Figures 3f and S32) than that of the hydrogenation steps in the pathway of NH_3 production, further in good accordance with the experimental results. On the other hand, we also studied the free-energy change of Cu_2O (111) (Figures 3e and S33), which was chosen to represent the reaction facets of Cu-RD-PBS. The ΔG_{*NOOH} of Cu (111) is −1.19 eV, which is lower than that of Cu_2O (111) (−0.81 eV). i.e. the alternative system with electrons localized at Cu_2O would rely on a 0.4 Volt higher reduction potential.

The advantage of the staged [2+6]-electron pathway for the NitrRR at low overpotentials also enables the exploration of NitrRR in a zinc-nitrate ($Zn–NO_3^-$) battery. A hybrid aqueous $Zn–NO_3^-$ battery catalyzed by Cu-RD-KOH electrode was assembled combined with a Zn anode (Figure 4a). Ideal $Zn–NO_3^-$ batteries in principle show a record high theoretical energy density of 943.2 Wh L^{-1} of the catholyte, based on the high solubility of NO_3^- in water (38 g/100 mL at 25 °C), and that each NO_3^- contributes on the cathode side to the storage of eight electrons (Figure 4b)

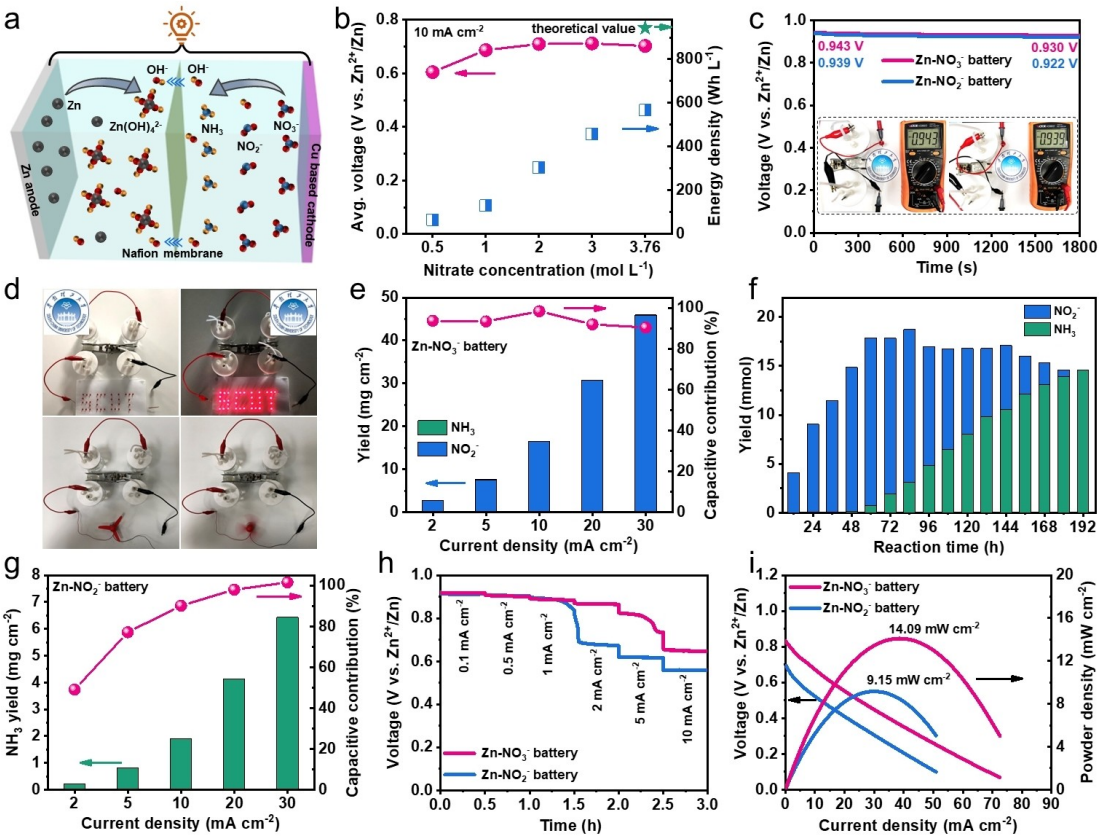

Figure 4. The electrochemical performance of hybrid aqueous $Zn–NO_3^-$ and $Zn–NO_2^-$ battery. a) The schematic illustration for assembled $Zn–NO_3^-$ and $Zn–NO_2^-$ battery with Zn anode and Cu-RD-KOH cathode. b) Average discharge voltage and corresponding energy density at different nitrate concentrations. c) Open-circuit voltage of $Zn–NO_3^-$ and $Zn–NO_2^-$ battery. d) In the case of power on and off, photographs of LEDs and a mini fan motor powered by the $Zn–NO_3^-$ battery. e) Yield and capacitive contribution of NO_2^- and NH_3 production for the $Zn–NO_3^-$ battery after a two-hour discharging process. f) Long-term discharge stability test of the $Zn–NO_3^-$ battery and corresponding yield at 20 mA cm^{-2}. g) Yield and capacitive contribution of NH_3 production for $Zn–NO_2^-$ battery after the two-hour discharging process. h) Comparison of rate performance of $Zn–NO_3^-$ battery through the two-electron process with $Zn–NO_2^-$ battery through the six-electron process. i) Discharging polarization curves and corresponding powder density curves of the $Zn–NO_3^-$ and $Zn–NO_2^-$ battery.

(that is one electron per 7.7 mass units, i.e. close to metallic Li). In our case, the NitrRR following a two-stage process is expected to lower the practical overpotential and to enlarge the extractable voltage of the battery. Typically, the voltage of Zn–NO_3^- battery stays around 0.70 V at 10 mA cm^{-2} (Figure S34), which lowers the calculated energy density to 566.7 Wh L^{-1} with 3.76 mol L^{-1} of NO_3^- in the electrolyte, being still much higher than that of other aqueous batteries, such as vanadium flow battery (25–35 Wh L^{-1}), Zn-Br_2 battery (65 Wh L^{-1}), lead battery (35–45 Wh L^{-1}) and Zn-I_2 battery (166.7 Wh L^{-1}) (Table S5).[17]

The performance metrics of battery were studied in detail taking an electrolyte with 0.5 M NO_3^- as an example. The Zn–NO_3^- battery shows an open-circuit voltage of 0.943 V (Figure 4c), which is closer to the theoretical voltage of 1.17 V. Two Zn–NO_3^- batteries in series can power 34 LEDs and a mini fan motor, respectively (Figures 4d, S35 and Video 1, 2), indicating practicability for energy supply. To further demonstrate the energy supply originating from the NitrRR, yields of NO_2^- and NH_3, and their corresponding relative contribution at different current densities were studied. For Zn–NO_3^- battery, first NO_2^- and not NH_3 was determined at a higher current density of 30 mA cm^{-2} after two-hour discharging, implying that the two-electron pathway initially plays a leading role in the discharging process, in perfect agreement with electrocatalysis experiments. (Figures 4e and S36, S37). The yield of NO_2^- increases in parallel with the current density and reaches the highest value of 45.9 mg cm^{-2} at 30 mA cm^{-2}, that is, the higher the current, the higher the nitrite production. The conversion of NO_3^- to NO_2^- contributes to more than 90 % of the liberated electrons when the current density exceeds 2 mA cm^{-2}, and the highest capacitive contribution of 98.3 % are achieved at a current density of 10 mA cm^{-2}. After first deloading the two electrons from the battery, a long-term discharging experiment was conducted to study if the other six electrons for the conversion of NO_2^- to NH_3 can be taken out, too, to realize the full potential of the Zn–NO_3^- battery. As shown in Figure 4f, NO_2^- yield quickly increases and reaches the maximum of 15.9 mmol when time goes up 72 hours at 20 mA cm^{-2}, which is equivalent to 80 % of the NO_3^- converted (Not including NH_3 production). Afterward, it gradually decreases to 0 after 192 hours. On the other hand, NH_3 was just detected after 60 hours and increased to 14.6 mmol after 192 hours. Therefore, our assembled Zn–NO_3^- battery allowed a staged [2+6]-electron discharging with a higher discharging voltage compared to the previously reported Zn–NO_3^- batteries (Figures S38 and S39).[9c,11a,18]

The six-electron discharging behavior of a Zn–NO_2^- battery was in detail studied as such after the total conversion of NO_3^- to NO_2^- intermediate. Zn–NO_2^- battery shows a high open-circuit voltage of 0.939 V (Figure 4c), being close to the theoretical potential of 1.12 V. The conversion of NO_2^- to NH_3 shows a nearly 100 % capacitive contribution at 20 and 30 mA cm^{-2} (Figures 4g and S40), indicating the six-electron transfer process could be successfully realized in the Zn–NO_2^- battery. The higher discharge voltage of Zn–NO_3^- battery during the early reaction period (where the conversion of NO_3^- to NO_2^- mainly happens) than that of Zn–NO_2^- battery across the entire current density range indicates again a stronger binding of nitrate when compared to nitrite (Figures 4h and S38, S41). A slight voltage decreased of Zn–NO_3^- battery in the second half of the period at 5 mA cm^{-2} is ascribed to the reduction reactions of copper oxide and nitrate is carried out simultaneously at the beginning of discharge process, and after a short period of electro-reduction the only reaction on the electrode surface is nitrate reduction, which results in a slight voltage decreased of battery. As a result, the Zn–NO_3^- battery reaches a maximal power density of 14.09 mW cm^{-2}, compared with the Zn–NO_2^- battery with a maximal power density of 9.15 mW cm^{-2} (Figure 4i). Importantly, the power density of both types of batteries is higher than recently reported state-of-the-art results using a direct eight-electron transfer process (< 6.0 mW cm^{-2}),[9c,11a,c,d,18] which further confirms the advantage of our catalyst.

In summary, we propose and demonstrate a clean copper catalyst electrode, which accesses a two-stage process to complete the [2+6]-electron reduction of NO_3^- to NH_3 by mimicking the optimized biological nitrate respiration. Our technical process is more effective than the previously reported systems operating by the direct eight-electron transfer process. The designed system with a relatively lower kinetic barrier obtains a FE of 91.5 % for NO_2^- formation and an FE of nearly 100 % for NH_3 synthesis at potentials of +0.2 V and +0.1 V *vs.* RHE, respectively. Such low overpotentials sum up to a low integrated energy consumption of 17.7 kWh kg^{-1} for ammonia production, comparable to that of the Haber-Bosch method. In addition, a Zn–NO_3^- battery designed with this electrode also follows the staged [2+6]-electron pathway at the cathodic side, providing an output voltage of 0.70 V and energy density of 566.7 Wh L^{-1} at 10 mA cm^{-2} as well as power density of 14.1 mW cm^{-2}, which are the highest values among the previously reported Zn–NO_3^- batteries. Therefore, this bio-inspired strategy based on designing a two-stage process for accelerating the kinetics of NitrRR enables an efficient and economical system simultaneously for on-site generation of ammonia from nitrate and remote energy supply. We assume that the system can be generalized to other multiple-electron-transfer reactions of non-metal salts.

Acknowledgements

This work was financially supported by the National Key R&D Program of China (Grant No. 2020YFB1505603), National Key R&D Program of China (Grant No. 2021YFB4000402), the Natural Science Foundation of China (22138005, 22141001), the Xplorer Prize and the Post-Doctoral Innovative Talents Project (BX20190119). We thank Shi-Yu Ren for her experimental assistance. We thank Guowei Weng and Sisi Wen for gas chromatography assistance. We gratefully acknowledge the Analysis & Testing Center at the South China University of Technology for ^{1}H NMR measurement. Open Access funding enabled and organized by Projekt DEAL.

Conflict of Interest

The authors declare no conflict of interest.

Data Availability Statement

The data that support the finding of this study are available from the corresponding author upon reasonable request.

Keywords: Ammonia Production · Cu Nanowires · Nitrate Reduction · Zn-Nitrate Battery · [2+6]-Electron Pathway

[1] a) J. G. Chen, R. M. Crooks, L. C. Seefeldt, K. L. Bren, R. M. Bullock, M. Y. Darensbourg, P. L. Holland, B. Hoffman, M. J. Janik, A. K. Jones, M. G. Kanatzidis, P. King, K. M. Lancaster, S. V. Lymar, P. Pfromm, W. F. Schneider, R. R. Schrock, *Science* **2018**, *360*, eaar6611; b) D. R. MacFarlane, P. V. Cherepanov, J. Choi, B. H. R. Suryanto, R. Y. Hodgetts, J. M. Bakker, F. M. Ferrero Vallana, A. N. Simonov, *Joule* **2020**, *4*, 1186–1205; c) C. H. Christensen, T. Johannessen, R. Z. Sørensen, J. K. Nørskov, *Catal. Today* **2006**, *111*, 140–144; d) O. Elishav, B. Mosevitzky Lis, E. M. Miller, D. J. Arent, A. Valera-Medina, A. Grinberg Dana, G. E. Shter, G. S. Grader, *Chem. Rev.* **2020**, *120*, 5352–5436; e) X. Guo, Y. Zhu, T. Ma, *J. Energy Chem.* **2017**, *26*, 1107–1116.

[2] C. Guo, J. Ran, A. Vasileff, S.-Z. Qiao, *Energy Environ. Sci.* **2018**, *11*, 45–56.

[3] a) G. F. Chen, S. Ren, L. Zhang, H. Cheng, Y. Luo, K. Zhu, L. X. Ding, H. Wang, *Small Methods* **2019**, *3*, 1800337; b) L. Wang, M. Xia, H. Wang, K. Huang, C. Qian, C. T. Maravelias, G. A. Ozin, *Joule* **2018**, *2*, 1055–1074; c) Y. Wang, Y. Yu, R. Jia, C. Zhang, B. Zhang, *Natl. Sci. Rev.* **2019**, *6*, 730–738.

[4] a) J. Zhang, Y. Ji, P. Wang, Q. Shao, Y. Li, X. Huang, *Adv. Funct. Mater.* **2020**, *30*, 1906579; b) J. Wang, L. Yu, L. Hu, G. Chen, H. Xin, X. Feng, *Nat. Commun.* **2018**, *9*, 1795; c) M. M. Shi, D. Bao, B. R. Wulan, Y. H. Li, Y. F. Zhang, J. M. Yan, Q. Jiang, *Adv. Mater.* **2017**, *29*, 1606550; d) G. F. Chen, A. Savateev, Z. Song, H. Wu, Y. Markushyna, L. Zhang, H. Wang, M. Antonietti, *Angew. Chem. Int. Ed.* **2022**, *61*, e202203170; *Angew. Chem.* **2022**, *134*, e202203170.

[5] a) S. Liu, M. Wang, H. Ji, X. Shen, C. Yan, T. Qian, *Natl. Sci. Rev.* **2021**, *8*, nwaa136; b) H. Shen, C. Choi, J. Masa, X. Li, J. Qiu, Y. Jung, Z. Sun, *Chem* **2021**, *7*, 1708–1754; c) S. Z. Andersen, V. Čolić, S. Yang, J. A. Schwalbe, A. C. Nielander, J. M. McEnaney, K. Enemark-Rasmussen, J. G. Baker, A. R. Singh, B. A. Rohr, M. J. Statt, S. J. Blair, S. Mezzavilla, J. Kibsgaard, P. C. K. Vesborg, M. Cargnello, S. F. Bent, T. F. Jaramillo, I. E. L. Stephens, J. K. Nørskov, I. Chorkendorff, *Nature* **2019**, *570*, 504–508.

[6] a) E. D. Glendening, A. M. Halpern, *J. Chem. Phys.* **2007**, *127*, 164307; b) R. Hawtof, S. Ghosh, E. Guarr, C. Xu, R. Mohan Sankaran, J. N. Renner, *Sci. Adv.* **2019**, *5*, eaat5778; c) J. Sun, D. Alam, R. Daiyan, H. Masood, T. Zhang, R. Zhou, P. J. Cullen, E. C. Lovell, A. R. Jalili, R. Amal, *Energy Environ. Sci.* **2021**, *14*, 865–872; d) L. R. Winter, J. G. Chen, *Joule* **2021**, *5*, 300–315; e) L. Li, C. Tang, X. Cui, Y. Zheng, X. Wang, H. Xu, S. Zhang, T. Shao, K. Davey, S. Z. Qiao, *Angew. Chem. Int. Ed.* **2021**, *60*, 14131–14137; *Angew. Chem.* **2021**, *133*, 14250–14256; f) Y. Ren, C. Yu, L. Wang, X. Tan, Z. Wang, Q. Wei, Y. Zhang, J. Qiu, *J. Am. Chem. Soc.* **2022**, *144*, 10193–10200; g) J. Long, S. Chen, Y. Zhang, C. Guo, X. Fu, D. Deng, J. Xiao, *Angew. Chem. Int. Ed.* **2020**, *59*, 9711–9718; *Angew. Chem.* **2020**, *132*, 9798–9805; h) R. Daiyan, T. Tran-Phu, P. Kumar, K. Iputera, Z. Tong, J. Leverett, M. H. A. Khan, A. Asghar Esmailpour, A. Jalili, M. Lim, A. Tricoli, R.-S. Liu, X. Lu, E. Lovell, R. Amal, *Energy Environ. Sci.* **2021**, *14*, 3588–3598.

[7] J. Li, J. Gao, T. Feng, H. Zhang, D. Liu, C. Zhang, S. Huang, C. Wang, F. Du, C. Li, C. Guo, *J. Power Sources* **2021**, *511*, 230463.

[8] a) J. Li, G. M. Zhan, J. H. Yang, F. J. Quan, C. L. Mao, Y. Liu, B. Wang, F. C. Lei, L. J. Li, A. W. M. Chan, L. P. Xu, Y. B. Shi, Y. Du, W. C. Hao, P. K. Wong, J. F. Wang, S. X. Dou, L. Z. Zhang, J. C. Yu, *J. Am. Chem. Soc.* **2020**, *142*, 7036–7046; b) S. G. Bratsch, *J. Phys. Chem. Ref. Data* **1989**, *18*, 1–21; c) J. M. McEnaney, A. R. Singh, J. A. Schwalbe, J. Kibsgaard, J. C. Lin, M. Cargnello, T. F. Jaramillo, J. K. Nørskov, *Energy Environ. Sci.* **2017**, *10*, 1621–1630; d) S. Giddey, S. P. S. Badwal, C. Munnings, M. Dolan, *ACS Sustainable Chem. Eng.* **2017**, *5*, 10231–10239.

[9] a) J. Yang, H. Qi, A. Li, X. Liu, X. Yang, S. Zhang, Q. Zhao, Q. Jiang, Y. Su, L. Zhang, J.-F. Li, Z.-Q. Tian, W. Liu, A. Wang, T. Zhang, *J. Am. Chem. Soc.* **2022**, *144*, 12062–12071; b) Y. Wang, W. Zhou, R. Jia, Y. Yu, B. Zhang, *Angew. Chem. Int. Ed.* **2020**, *59*, 5350–5354; *Angew. Chem.* **2020**, *132*, 5388–5392; c) Y. Guo, R. Zhang, S. Zhang, Y. Zhao, Q. Yang, Z. Huang, B. Dong, C. Zhi, *Energy Environ. Sci.* **2021**, *14*, 3938–3944; d) Z.-Y. Wu, M. Karamad, X. Yong, Q. Huang, D. A. Cullen, P. Zhu, C. Xia, Q. Xiao, M. Shakouri, F.-Y. Chen, J. Y. Kim, Y. Xia, K. Heck, Y. Hu, M. S. Wong, Q. Li, I. Gates, S. Siahrostami, H. Wang, *Nat. Commun.* **2021**, *12*, 2870.

[10] a) J. J. M. Isabel Moura, *Curr. Opin. Chem. Biol.* **2001**, *5*, 168–175; b) A. M. Oliver Einsle, P. Stach, G. P. Bourenkov, Hans D. Bartunik, R. Huber, P. M. H. Kroneck, *Nature* **1999**, *400*, 476–480; c) S. Durand, M. Guillier, *Front. Mol. Biosci.* **2021**, *8*, 667758.

[11] a) R. Zhang, Y. Guo, S. Zhang, D. Chen, Y. Zhao, Z. Huang, L. Ma, P. Li, Q. Yang, G. Liang, C. Zhi, *Adv. Energy Mater.* **2022**, *12*, 2103872; b) H. Du, H. Guo, K. Wang, X. Du, B. A. Beshiwork, S. Sun, Y. Luo, Q. Liu, T. Li, X. Sun, *Angew. Chem. Int. Ed.* **2023**, *62*, e202215782; *Angew. Chem.* **2023**, *135*, e202215782; c) Z. Li, Z. Deng, L. Ouyang, X. Fan, L. Zhang, S. Sun, Q. Liu, A. A. Alshehri, Y. Luo, Q. Kong, X. Sun, *Nano Res.* **2022**, *15*, 8914–8921; d) R. Zhang, S. Zhang, Y. Guo, C. Li, J. Liu, Z. Huang, Y. Zhao, Y. Li, C. Zhi, *Energy Environ. Sci.* **2022**, *15*, 3024–3032.

[12] a) P. Li, Z. Jin, Z. Fang, G. Yu, *Energy Environ. Sci.* **2021**, *14*, 3522–3531; b) F.-Y. Chen, Z.-Y. Wu, S. Gupta, D. J. Rivera, S. V. Lambeets, S. Pecaut, J. Y. T. Kim, P. Zhu, Y. Z. Finfrock, D. M. Meira, G. King, G. Gao, W. Xu, D. A. Cullen, H. Zhou, Y. Han, D. E. Perea, C. L. Muhich, H. Wang, *Nat. Nanotechnol.* **2022**, *17*, 759–767; c) S. Zhang, M. Li, J. Li, Q. Song, X. Liu, *Proc. Natl. Acad. Sci. USA* **2022**, *119*, e2115504119; d) W. He, J. Zhang, S. Dieckhöfer, S. Varhade, A. C. Brix, A. Lielpetere, S. Seisel, J. R. C. Junqueira, W. Schuhmann, *Nat. Commun.* **2022**, *13*, 1129; e) G.-F. Chen, Y. Yuan, H. Jiang, S.-Y. Ren, L.-X. Ding, L. Ma, T. Wu, J. Lu, H. Wang, *Nat. Energy* **2020**, *5*, 605–613; f) X. Wang, M. Zhu, G. Zeng, X. Liu, C. Fang, C. Li, *Nanoscale* **2020**, *12*, 9385–9391.

[13] a) J. r. Simon, *FEMS Microbiol. Rev.* **2002**, *26*, 285–309; b) M. Duca, M. T. M. Koper, *Energy Environ. Sci.* **2012**, *5*, 9726; c) C. B. Pandey, U. Kumar, M. Kaviraj, K. J. Minick, A. K. Mishra, J. S. Singh, *Sci. Total Environ.* **2020**, *738*, 139710.

[14] a) Y. Wang, R. Shen, X. Jin, P. Zhu, Y. Ye, Y. Hu, *Appl. Surf. Sci.* **2011**, *258*, 201–206; b) Q. Zhang, J. Wang, D. Xu, Z. Wang, X. Li, K. Zhang, *J. Mater. Chem. A* **2014**, *2*, 3865–3874.

[15] T. Hu, C. Wang, M. Wang, C. M. Li, C. Guo, *ACS Catal.* **2021**, *11*, 14417–14427.

[16] a) N. C. Kani, J. A. Gauthier, A. Prajapati, J. Edgington, I. Bordawekar, W. Shields, M. Shields, L. C. Seitz, A. R. Singh,

M. R. Singh, *Energy Environ. Sci.* **2021**, *14*, 6349–6359; b) Y. Wang, D. Wu, P. Lv, B. He, X. Li, D. Ma, Y. Jia, *Nanoscale* **2022**, *14*, 10862–10872.

[17] a) E. Sánchez-Díez, E. Ventosa, M. Guarnieri, A. Trovò, C. Flox, R. Marcilla, F. Soavi, P. Mazur, E. Aranzabe, R. Ferret, *J. Power Sources* **2021**, *481*, 228804; b) B. Li, Z. Nie, M. Vijayakumar, G. Li, J. Liu, V. Sprenkle, W. Wang, *Nat. Commun.* **2015**, *6*, 6303; c) J. O. G. Posada, A. J. R. Rennie, S. P. Villar, V. L. Martins, J. Marinaccio, A. Barnes, C. F. Glover, D. A. Worsley, P. J. Hall, *Renewable Sustainable Energy Rev.* **2017**, *68*, 1174–1182.

[18] Q. Liu, L. Xie, J. Liang, Y. Ren, Y. Wang, L. Zhang, L. Yue, T. Li, Y. Luo, N. Li, B. Tang, Y. Liu, S. Gao, A. A. Alshehri, I. Shakir, P. O. Agboola, Q. Kong, Q. Wang, D. Ma, X. Sun, *Small* **2022**, *18*, 2106961.

Manuscript received: December 18, 2022
Accepted manuscript online: February 2, 2023
Version of record online: February 16, 2023